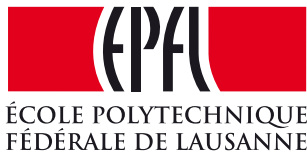


# Atomistic modeling of solid–liquid interface of metals and alloys out of equilibrium

An overview of the state of the art



**Candidate:** Edoardo Baldi

**Thesis director:** Prof. Michele Ceriotti

Laboratory of Computational Science and Modeling  
École Polytechnique Fédérale de Lausanne

Lausanne – June 28, 2016



# Contents

<b>1</b>	<b>Introduction</b>	<b>1</b>
<b>2</b>	<b>Simulating additive manufacturing</b>	<b>3</b>
2.1	Present simulation approaches and challenges . . . . .	3
2.2	Focus on interfacial properties . . . . .	5
<b>3</b>	<b>The capillary fluctuation method revisited</b>	<b>9</b>
3.1	The method . . . . .	9
3.2	Results . . . . .	14
<b>4</b>	<b>Modeling atomistic interactions</b>	<b>19</b>
4.1	The embedded atom method . . . . .	19
4.2	Applications to alloys . . . . .	21
<b>5</b>	<b>Outlook</b>	<b>25</b>
5.1	CFM out of equilibrium . . . . .	25
	<b>Bibliography</b>	<b>27</b>



# 1 | Introduction

The term “additive manufacturing” (AM) can be considered as an evolution of the “rapid prototyping” process, used in various industries to indicate a process of rapidly creating a system or part of it before the final release and commercialization (i.e. a prototype). However, recently a significant improvement in the output of these processes has shown that there is a much closer link with the final product and the new name of “additive manufacturing” has been chosen.

In few words, the basic feature of the AM technology is the possibility to design an object of interest by means of a 3D Computer Aided Design software and then fabricate it directly with almost no need of process planning. Though a very complicated process, AM has the advantage to significantly simplify the work of producing complex 3D objects directly from a software project. Other manufacturing process would require a detailed analysis of the object to determine, for example, the order in which each part has to be built and also the assembly phase.

AM technologies have been described as a very revolution in product development and manufacturing; final products obtained with AM suggest that this technology could actually redefine what we mean today by a “manufacturing process”. In order to (try to) explain these enthusiastic forecasts, we need to remark what are the advantages of AM technologies. First, we should emphasize again the “rapid” character of this process: it is not just in term of time needed to build an object, but all the development process experiences a speedup, mainly because we are using computers throughout.

Secondly, there is a reduction in the number of process steps, despite the possible complexity of final objects. AM is usually involves one single step, while standard manufacturing processes would require a particular sequence of multiple and/or iterative steps to be carried out: even a relatively simple change in the project may require significant modification in the fabrication process and, in turn, an increase in the time required to obtain the final product.

The current research focus of AM techniques is to produce complex shaped functional metallic components in order to meet the demanding requirements of several important industrial sectors, such as aerospace, biomedical and rapid tooling. For the fabrication of these components to be cost effective and as accurate as possible, three typical laser based processes have been developed: *laser sintering* (LS), *laser melting* (LM) and *laser metal deposition* (LMD). Our research interest will be focused on LM (also called *selective laser melting*), mainly because all the companies involved in the project operate with this specific fabrication process.

The present research plan begins with an detailed state-of-the-art review of the additive man-

## Chapter 1. Introduction

---

ufacturing technology, together with its challenges and fields where advanced computer simulations can give precious insights. To this end, it will be addressed the study of fundamental bulk properties of real systems (metals and alloys) useful both at the industrial and research level. More complex phenomena like interface properties will be initially investigated on simple systems and, concurrently, part of the work will be dedicated to the development of more reliable and flexible interatomic potentials, with which eventually we would like to shed light on these complex phenomena in relevant systems.

## 2 | Simulating additive manufacturing

### 2.1 Present simulation approaches and challenges

As a whole, AM processes are considered as an important step-change in manufacturing technologies nowadays widely used, opening up the possibility of going almost directly from Computer Aided Design to net-shape defined products. With sufficient penetration in the industrial sector, this kind of technology could have a significant impact on both the environment and on sustainable manufacturing, with large reduction of material wastage and integrated components with specific optimized features. However, there are many challenges to be overcome to increase the importance of these technologies for the industry. These range from business considerations to technical and inherent differences in the processes from industry standards. Computational modeling has a relatively important role to play in addressing these issues, when compared with its role in other manufacturing processes. An interesting aspect of AM from the perspective of computational modeling regards the manufacturing length scales. In a conventional casting process, for example, the local cooling rates are determined on a macroscale, thus directly linked to the size of the casting. All the phenomena occurring during such a process usually spread across a broad length scale, making a multi-scale simulation approach a rather challenging task. On the other hand, the manufacturing length scales of powder through AM processes are much smaller and closely related to the size of the melt pool; also, solidification cooling rates are much higher. Thus, in a multi-scale simulation, the linking across the length scales could be more achievable by common modeling techniques such as finite elements or phase field simulations, both of which can guide the fabrication process to obtain components with designed features (e.g. microstructures, mechanical properties, etc.).

With the aid of computational modeling, there are several key areas which are subject of research interests, namely:

- thermal modeling of melting and solidification;
- residual stress modeling;
- topological and shape optimization of components.

Among these topics, the first one regarding the fundamental phenomena of melting and solidification is by far the most important. Also, analysis of residual stresses has its starting point with the thermal history of the processed component. Besides meso-scale approaches useful to bridge the gap between the modeling phase and actual industrial fabrication, also simulation techniques at the atomic scale can give valuable insights when trying to better understand complicate processes of AM.

There are several motivations to employ atomistic simulations to study materials under the conditions they are subject to during AM processes. The foremost reason is related to the out-of-equilibrium conditions that are usually the “scenario” in which additive manufacturing takes place: we already mentioned the importance of this kind of phenomena that occur away from thermodynamical equilibrium (see Section 2.1). Thus, atomistic simulations are the most predictive method to investigate these aspects.

### 2.1.1 Open issues

Among particular properties of interests for all AM processes, there are microstructural and mechanical properties and the out of equilibrium phenomenon known as solute trapping. The first two are of primary importance for AM applications and, at the same time, they represent quite broad classes of materials properties. Solute trapping is of peculiar interest when studying solid-liquid interfaces, especially when dealing with multi-component systems (e.g. ternary or more complex alloys).

Mechanical properties of AM processed components are strongly linked to the solidification microstructure. The high-energy laser interaction gives rise to a very fast heating and melting of materials, which is inevitably followed by a rapid solidification on cooling. Laser-based AM processes normally offer high heating and cooling rates ( $\sim 100$  K/s) [1] at the solid-liquid interface, producing a molten pool of quite small size ( $\sim 1$  mm) [2]. Furthermore, the rates of quenching that occur by conduction of heat through the substrate are fast enough to produce a rapid solidification microstructure. Therefore, as a characteristic of AM processed materials, grain refinement is generally expected, due to an insufficient time for grain development and growth. Moreover, either chemical concentration or temperature gradients in the molten pool may generate surface tension gradient, making the solidification a non-steady state process (due to the so-called “Gibbs-Marangoni effect”). On the other hand, rapid solidification has the kinetic limitation of crystal growth that normally follows the direction of maximum heat flow. The simultaneous but competitive action of the above two mechanisms, i.e. a non-equilibrium solidification nature and a localized directional growth tendency, may lead to a variety of crystal orientations with a short-range regularity [3]. Therefore, metallic materials processed by AM may present intrinsic, more or less, anisotropic features.

Another important issue concerning mechanical properties of AM-processed materials is related to the residual stresses (i.e. stresses that remain inside a material, when it has reached equilibrium with its environment) that arise in the parts being produced. Residual stresses may impose some serious limitations to the practical use, since they introduce part deformations and/or micro cracks. Moreover, large residual stresses can limit the load resistance of the parts compared to a stress-free state.



Among material properties the elastic modulus and the coefficient of thermal expansion play an important role in what determines the level of residual stresses. The elastic modulus is of primary importance when phase transformations take place, as they may be detrimental or beneficial with respect to residual stresses. Normally, the formation of brittle phases during AM may promote stress cracking, whereas some controlled phase transformations may have the potential to reduce or eliminate stresses and deformation.

Laser processing conditions can be tuned to control the presence of residual stresses. For LS and LM processes, the laser scanning strategy has a significant influence on the residual stresses being developed. Normally, the stresses are larger perpendicular to the scan direction than along the scan direction [4] and a subdivision of the surface in smaller sectors has been shown to lead to a lower stress value.

## 2.2 Focus on interfacial properties

During first-order phase transition such as nucleation and growth, interfacial properties play a central role. In particular, the interfacial free energy between the solid and the liquid phase (usually indicated with  $\gamma_{sl}$ ) controls the barrier for nucleation of solid in an undercooled liquid and the crystal growth, which can present different regimes: planar, cellular and dendritic, the latter of particular interest for metals.

Despite its importance from both theoretical models and practical applications, an accurate calculation of  $\gamma_{sl}$  is a rather complicated task even for the case of simple elements. Furthermore, on the experimental side, few techniques aimed at measuring this quantity are complicated by the very strict control on all experimental parameters that must be achieved to obtain accurate data. One method, for example, involves recovering  $\gamma_{sl}$  from nucleation-rate measurements: in this particular case, a major difficulty arises from the possible occurrence of heterogeneous nucleation from very low-concentration of impurities.

Several computational methods have been developed to calculate  $\gamma_{sl}$ , where a complete control on the experimental variables is possible. These methods are the *capillary fluctuation method* (CFM), different sorts of so-called *cleaving methods* (CMs) and approaches based on *classical nucleation theory* (CNT). All these schemes largely rely on molecular dynamics in conjunction with Monte Carlo simulations.

Recently, approaches of this kind coupled with the accelerated sampling technique of metadynamics have been presented: the key idea is to obtain  $\gamma_{sl}$  from a free-energy map of the phase transition reconstructed by metadynamics [5], allowing also to investigate solidification and melting in out-of-equilibrium conditions [6], much more relevant for experiments and mesoscale models of solidification (including additive manufacturing processes).

### 2.2.1 Capillary fluctuations and free energies

The capillary fluctuation method was firstly introduced by Asta and coworkers [7] in 2001 and employs an analysis of height fluctuations of the solid-liquid interface at equilibrium to extract the interface stiffness,  $\sigma$ .

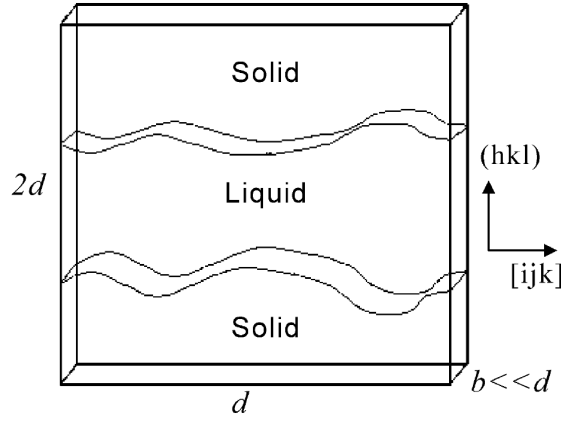


Figure 2.1: Schematic model of the one dimensional system considered in the original work on the capillary fluctuation method [10].

In purely mathematical terms, the stiffness can be defined as the second-order coefficient of the power expansion of the free energy with respect to orientation. In this context, orientation means an instantaneous angle (or two of those if we deal with a 2D surface, as explained later) by which the normal of the interface is tilted with respect to the axes of the chosen coordinate system (usually a Cartesian system). From a physical point of view, the stiffness is related to the energy cost of bending the surface.

The approach of CFM has been successfully applied to derive interfacial free energies from atomistic simulations for the liquid–vapor surface of Lennard–Jones system [8] and for amorphous polymer films [9], just to mention a couple of examples.

The CFM starts with crystal–liquid systems that have been equilibrated at the melting point using molecular dynamics for pure materials or Monte Carlo simulations necessary to study alloys. To minimize the number of atoms, typical simulation cells are chosen to be quasi-two dimensional, with the length of the interface  $d$  much larger than the thickness of the system,  $b$  (see Fig. 2.1). The length  $d$  is chosen sufficiently large to allow measurement of capillary fluctuation amplitudes over a wide range of wavelengths.

Since periodic boundary conditions are applied, two identical interfaces are present in a simulation box. Thus, to avoid unwanted interactions between the two interfaces, the length of the simulation cell parallel to the interface normal is chosen to be of the order of  $2d$ .

In short, CFM is based upon collecting snapshots of the system during the simulation and for each of them measure the squared amplitude of capillary fluctuations. At the end of the simulation, an ensemble average is computed to obtain the mean value of the amplitudes: this term is directly related to the interfacial stiffness. In this context, the stiffness  $\sigma$  is defined as  $\gamma + \gamma''_{\theta}$ , where  $\gamma''_{\theta}$  denotes the second derivative of the interfacial free energy with respect to the orientational angle  $\theta$ , that is the angle between the local normal to the solid–liquid interface and the average orientation for the reference flat interface. The key point of this approach is that the stiffness is one order of magnitude more anisotropic than the free energy itself, thus it can be computed more easily with smaller errors.

The CFM exploits the well-known result from capillary theory [11] for which the stiffness is

directly related to the equilibrium fluctuation spectrum of a rough interface. In mathematical terms, for a quasi-two dimensional interface, this reads

$$\langle |A(k)|^2 \rangle = \frac{k_B T_m}{S(\gamma + \gamma''_{\theta})k^2}, \quad (2.1)$$

where  $S$  is the cross sectional area of the interface and  $T_m$  the melting temperature.  $A(k)$  is the amplitude of an height perturbation of the interface with wavelength  $\lambda = 2\pi/k$  much larger than the lattice spacing. In other words, the terms denoted by  $A(k)$  for different wave vectors  $k$  are the coefficients of the Fourier expansion of the height function,  $h(x)$

$$h(x) = \sum_k A(k) \exp(ikx). \quad (2.2)$$

The quantities  $\gamma$  and  $\gamma''_{\theta}$  in the denominator of Eq. 2.1 originate from the energy cost of bending locally the interface away from its mean orientation, which is why the fluctuation spectrum measures directly the interface stiffness.

At this point, a fundamental question that arises is related to the method needed to construct the height function  $h(x)$ . To answer this question, one need to know a way of locating the interface during the simulation. To this end, the vast majority of scientific literature of CFM exploits some kind of local structural order parameter which is able to distinguish between solid and liquid atoms. Through the use of such order parameter, the position of the interface can be identified as a function of the distance along the interface (i.e.  $x$  in this one-dimensional case, but in the most general case, one would have a function  $h(x, y)$  of the two coordinates parallel to the interface). An in depth description of the way we adopted to be able to distinguish solid and liquid phases and to locate the instantaneous position of the interface will be given in the next chapter.

With the “recipe” given by Eq. 2.1 and Eq. 2.2, the CFM is used to derive values of the stiffness for several interface orientations and the results are then combined with an analytical expansion of the interface free energy  $\gamma(\hat{n})$  to map out the full anisotropy of the solid-liquid interfacial free energy. For the applications considered here, the appropriate expansion for  $\gamma(\hat{n})$  involves cubic harmonics, that are linear combinations of spherical harmonics that obey the cubic symmetry of the lattice. Following the approach developed by Fehner [12], the expansion for the interface free energy is

$$\frac{\gamma(\hat{n})}{\gamma_0} = 1 + \epsilon \left( \sum_{i=1}^3 n_i^4 - \frac{3}{5} \right) + \delta \left( 3 \sum_{i=1}^3 n_i^4 + 66n_1^2 n_2^2 n_3^2 - \frac{17}{7} \right) + \dots \quad (2.3)$$

where  $\hat{n} = (n_1, n_2, n_3)$  is the interface normal and the parameters  $\epsilon$  and  $\delta$  give a measure of the anisotropy of  $\gamma$ .

With the relation of Eq. 2.1 and the expansion of Eq. 2.3, three different calculations for independent interfaces are needed to obtain the parameters of the expansion ( $\gamma_0$ ,  $\epsilon$  and  $\delta$ ). In a more recent work on dendritic growth in metals, Becker et al. [13] made use of different simulations geometries containing two-dimensional interfaces, instead of the so far discussed “quasi” two-

## Chapter 2. Simulating additive manufacturing

---

dimensional. In this case, one must fully take into account the possibility of capillary waves also in the other direction parallel to the interface and the relation between amplitudes of capillary fluctuations and wave vectors becomes

$$\langle |A(k_x, k_y)|^2 \rangle = \frac{k_B T_m}{S(\sigma_{11}k_x^2 + \sigma_{22}k_y^2 + 2\sigma_{12}k_x k_y)}. \quad (2.4)$$

Although these 2D simulation geometries require larger cells and in turn more atoms, there is the advantage that from two independent interface normals (due to symmetry arguments, as explained in the following), three independent stiffness values can be obtained and so only two simulations are needed to fully parametrize  $\gamma$ . Moreover, more  $k$  modes are accessible from a 2D interface, because wave vectors have the form  $2\pi(j_1/L_1, j_2/L_2)$ , where  $L_1$  and  $L_2$  are the lengths of the simulation box along the interface and  $j_1, j_2$  are two non-zero indexes.

For 2D interfaces, the stiffness  $\sigma$  is a second-order tensor with three independent values in general<sup>1</sup>, but symmetry arguments can reduce the independent values for certain interface orientations. For example, for a (100) interface in a FCC crystal, if two of the Cartesian axes are along [100] and [010] directions, the off-diagonal terms are zero and the diagonal terms are equal. In this case, the general relation of Eq. 2.4 is similar to the equation for the 1D geometry, but it is important to stress that  $\gamma$  can still be parametrized with two independent interfaces: the fact that the stiffness tensor reduces to a single component is purely a consequence of symmetry.

---

<sup>1</sup>This is true on general grounds because of the definition of the stiffness as second-order derivative of the interface free energy with respect to the orientational angles:

$$\sigma_{ij} = \frac{\partial^2 \gamma}{\partial \theta_i \partial \theta_j}.$$

## 3 | The capillary fluctuation method revisited

As discussed in detail in the previous chapter (Section 2.2.1), the capillary fluctuation method is a technique that can be essentially divided in four “steps”.

1. **Defining an appropriate way to discriminate solid and liquid.** This is the very first step since the next goal will be that of “locating” in an atomistic system the dividing surface between the solid and the liquid phase.
2. **Analysing the surface profile.** At this point we are able to distinguish atoms that belong to a solid-like environment and liquid-like ones; we can track down the position of the surface by collecting snapshots of its profile,  $h$ . The latter is in general a function of two variables, i.e. the coordinates (with respect to the chosen coordinate system) in the interface plane. At the end of the simulation, the profile function  $h$  is Fourier transformed and an ensemble average is computed to obtain the so-called fluctuations spectrum.
3. **Fitting the fluctuations spectrum.** Relations such as Eqs. (2.1) and (2.4) give the explicit link between capillary fluctuations and surface stiffness  $\sigma$ . Through the fit of these non-linear models for different surfaces, we are able to completely determine the  $\sigma$  tensor.
4. **Extracting the anisotropy coefficients.** Since we know the relation between interface free energy and the stiffness and we have an approximation of the anisotropy of  $\gamma$ , we can analytically determine  $\sigma$  from Eq. (2.3) and fit this against the value of the stiffness calculated previously. In this way we will obtain the two anisotropy coefficients (here  $\epsilon$  and  $\delta$ ) and completely map out the dependence of  $\gamma$  from the interface orientation.

### 3.1 The method

In this section we explain in full detail all the aforementioned steps, which build the framework of capillary fluctuation method we adopted for our calculations of the stiffness for a Lennard-Jones system, devoting more attention to substantial differences with the original method developed by Asta.

### 3.1.1 Solid or liquid

As it has already been stressed, the very first requirement for a computational method whose aim is to study phase transitions or coexistence between different phases is a way of distinguishing particles belonging to the phases involved<sup>1</sup>.

In molecular simulations of this kind, it is widespread to make use of a more or less complicate function that depends on atomic coordinates and that can give a quantitative indication of the “order” of one atom’s neighborhood: this class of functions are usually called *order parameters*. Many of these functions have been developed in order to face different problems; probably, the most known order parameters are the *Steinhardt–Nelson* functions of different orders:  $Q_3$ ,  $Q_4$  and  $Q_6$  [14].

A common feature of all these order parameters is that they are some sort of average computed considering the coordinates of all the atoms and it should be intuitive that no function of this type is able to distinguish, for example, all the crystalline phases of a given system if they have different symmetry. In other words, a certain choice of an order parameter might be more suitable than another if one wants to study the environment of an HCP crystal rather than an FCC one. Since all our systems (Lennard–Jones and real metal alloys) show at least one FCC crystalline phase, we chose the order parameter adopted also by Angioletti–Uberti [5] and BCheng [6] in their metadynamics calculations of interface free energy. This order parameter (henceforth called FCCUBIC,  $\Phi$ ) is defined as

$$\Phi(\mathbf{x}_i) = \frac{\sum_{j \neq i} C_r(|\mathbf{x}_j - \mathbf{x}_i|) C_\alpha(\mathbf{x}_j - \mathbf{x}_i)}{\sum_{j \neq i} C_r(|\mathbf{x}_j - \mathbf{x}_i|)}. \quad (3.1)$$

The FCCUBIC order parameter is a weighted average running over all pairs of atoms of an angular term ( $C_\alpha$ ) and a “weight” which is a radial cutoff function ( $C_r$ ) that ensures that  $\Phi$  is a continuous function of all its arguments. The angular part can be specified using a set of Euler angles (by means of a Euler rotation matrix  $\mathbf{R}$ ) and can be written as

$$C_\alpha^{(\varphi, \psi, \theta)}(\mathbf{r}_{ij}) = C_\alpha(\mathbf{R}^{(\varphi, \psi, \theta)} \cdot \mathbf{r}_{ij}). \quad (3.2)$$

Advantages of FCCUBIC order parameter over the mentioned Steinhardt’s  $Q$  functions are, mainly: the angular part  $C_\alpha$  has well-defined peaks for the FCC environment; it is not rotationally invariant and thus it is able to recognize crystal orientations consistent with the imposed periodic boundary conditions; it is relatively cheap to compute. It is possible to construct a different form of  $C_\alpha$  if one wanted to deal with a different crystal structure, and one simply has to rotate the function through the Euler matrix  $\mathbf{R}$  in order to specify a different crystallographic orientation of the surface. The possibility of having an orientation-dependent order parameter is an essential ingredient of our method.

The “final”  $\Phi$  actually used in our simulations is subject to few other mathematical manipulations mainly aimed to obtain that the perfect FCC lattice corresponds to  $\Phi = 1$ , while the

---

<sup>1</sup>Here we restrict ourselves to the case of solid and liquid, but it is clear that this prerequisite is completely general.

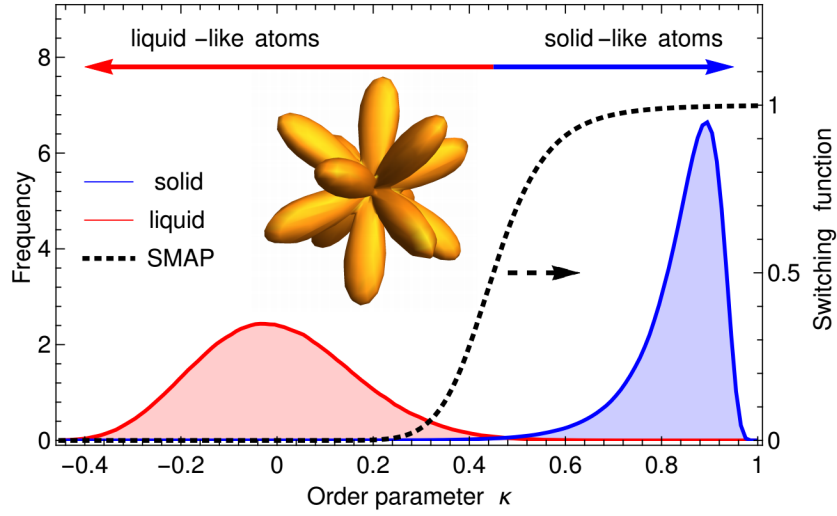


Figure 3.1: The distributions of the FCCUBIC order parameter for a bulk FCC crystal oriented with  $\langle 100 \rangle$  directions parallel to the axes of the simulation cell. The distributions are computed at the equilibrium melting temperature. The dashed line is a plot of the switching function applied [6].

average value for atoms in bulk liquid is zero<sup>2</sup>. Lastly, since the distributions of such order parameter for a bulk solid system and a bulk liquid have a minimal amount of overlap (see Fig. 3.1), a non-linear switching function is applied to  $\Phi$  in order to have a tunable and smooth variation from solid-like region to liquid-like<sup>3</sup>.

### 3.1.2 Looking for the dividing surface

In the work of Asta et al. they obtained the profile function of the dividing surface in the following way: they computed an FCC order parameter defined as  $\phi = (1/12) \sum_i |\mathbf{r}_i - \mathbf{r}_{fcc}|^2$ , where  $\mathbf{r}_{fcc}$  is the distance between the central atom  $i$  and its first 12 neighbours in the given orientation. Then, the  $x$  direction in the simulation cell, parallel to the interface, is divided into slices and  $\phi$  averaged over the slice is computed as a function of the  $y$  direction (along the normal of the interface). As the solid-liquid interface is crossed, the value of  $\phi$  changes abruptly and the interface can be accurately located. By collecting snapshots of this function

<sup>2</sup>This is ensured by applying a linear scaling of the kind

$$\Phi(i) = \frac{\Phi^0(i) - \Phi_l^0}{\Phi_s^0 - \Phi_l^0},$$

where  $s$  and  $l$  indicate the average of  $\Phi$  on a bulk solid and liquid system respectively, and  $\Phi^0$  is the unscaled order parameter defined above.

<sup>3</sup>In this case, the non-linear switching function applied has the form

$$s(r) = \left[ 1 + (2^{a/b} - 1) \left( \frac{r - d_0}{r_0} \right)^a \right]^{-b/a},$$

where  $r_0$  and  $d_0$  are tunable parameters. For  $r \leq d_0$   $s(r) = 1$ , while for  $r > d_0$  the function decays smoothly to 0.

during all the simulation, one ends up with the time-varying profile function  $h(y, t)$ , where both the space and time coordinates are discretized.

The discrete nature of the profile function stems directly from the fact that the order parameter is a discrete quantity, since it assigns a numerical value to each atom. In turn, it means that the representation of the surface built in this way is highly sensitive on the  $x$ -width of the slices over which  $\phi$  is averaged (i.e. the bin size).

In our approach, we followed the idea proposed by Willard and Chandler [15]. To identify the liquid-vapour interface in water systems such that the resulting surface is to all effects a continuous function, they built a coarse-grained density field by computing the convolution of the instantaneous density field with a chosen kernel function. In this case, the kernel functions are taken to be normalized Gaussians, which depend on one parameter ( $\xi$ , the Gaussian width). So, in mathematical terms

$$\begin{cases} \rho(\mathbf{r}, t) = \sum_i \delta(\mathbf{r} - \mathbf{r}_i(t)) \\ \kappa(\mathbf{r}; \xi) = (2\pi\xi^2)^{-d/2} \exp(-r^2/2\xi^2) \end{cases} \xrightarrow{\text{convolution}} \bar{\rho}(\mathbf{r}, t) = \sum_i \kappa(|\mathbf{r} - \mathbf{r}_i(t)|; \xi) \quad (3.3)$$

Here  $r$  is the magnitude of the distance vector  $\mathbf{r}$  and  $\xi$  is the coarse-graining length;  $d$  stands for the dimensionality of the system. As we will discuss in the Results section, the importance of  $\xi$  is that it controls the coarse nature of the continuous field obtained and it has to be chosen according to physical conditions under consideration.

From this idea for a simple density field to an *order parameter density field*, the step is really short: it suffices modifying the instantaneous atomistic “density” as follows

$$\rho(\mathbf{r}, t) \rightsquigarrow \rho_\phi(\mathbf{r}, t) = \sum_i \phi_i \delta(\mathbf{r} - \mathbf{r}_i(t)), \quad (3.4)$$

and the coarse-grained field needs to be properly normalized

$$\bar{\rho}_\phi(\mathbf{r}, t) = \frac{\sum_i \phi_i \kappa(|\mathbf{r} - \mathbf{r}_i(t)|; \xi)}{\sum_i \kappa(|\mathbf{r} - \mathbf{r}_i(t)|; \xi)}. \quad (3.5)$$

Once  $\xi$  is set, the dividing surface is defined to be the  $(d - 1)$ -dimensional manifold  $\mathbf{r} = \mathbf{s}$  for which

$$\bar{\rho}_\phi(\mathbf{s}, t) = C, \quad (3.6)$$

where  $C$  is some constant value. In other words, the instantaneous interface between solid and liquid is the locus of points in space where the order parameter density field assumes the value of  $C$  (sometimes called *isovalue*). It is clear that the choice of this constant is arbitrary, but it should rely on some meaningful physical consideration. Since the coarse-grained field changes with time as molecular configurations change, the surface is a two-dimensional function which depends on time only through atomic coordinates:  $\mathbf{s}(t) = \mathbf{s}(\{\mathbf{r}_i(t)\})$ .

For a given molecular configuration  $\{\mathbf{r}_i\}$  at time  $t$ , Eq. (3.6) can be solved quickly with a variety of numerical algorithms, for example through interpolation on a spatial grid. If this equation



is recast in the form  $\bar{\rho}_\phi(\mathbf{r}, t) - C = 0$ , one among all the known root-finding algorithms can be exploited to solve it. We adopted the method due to Brent and Dekker<sup>4</sup>, which has the reliability of the bisection method, but it is faster in convergence.

Once an entire simulation for a specific interface is analysed, the interface profile function is Fourier transformed to obtain its fluctuation spectrum. Practical details of the simulations will be given in the next section; here it is sufficient to note that we employed the 2D geometry so that we needed only two independent surfaces to get the full anisotropy through the stiffness tensor. To get fluctuations amplitudes that appears in Eq. (2.4),  $h(\mathbf{x})$ , where  $\mathbf{x}$  is the vector with components  $(x, y)$ , is Fourier transformed according to

$$h(\mathbf{x}, t) = \sum_{\mathbf{k}} A(\mathbf{k}, t) \exp(i\mathbf{k} \cdot \mathbf{x}), \quad (3.7)$$

and  $\mathbf{k}$  is the wave vector which takes the form  $2\pi(j_x/L_x, j_y/L_y)$ , with  $j_x, j_y$  being non zero indexes and  $L_x, L_y$  the size of the simulation cell in the interface plane.

The last step is to compute the ensemble (time) average of the fluctuation spectrum<sup>5</sup>, where with “spectrum” we refer to the square moduli of the complex Fourier amplitudes.

One last detail is necessary to discuss: how to fix the constant value  $C$  in order to solve Eq. (3.6). In the original paper where this method was introduced, the authors were using the method to provide useful and instructive pictures of liquid–vapour and liquid–protein interfaces, particularly with water. For the case of the liquid–vapour dividing surface, they fixed the constant to one-half the density of liquid water in their system.

In our case, a physically reasonable value for the constant would be the one that could clearly discriminate between a particle in a solid-like environment from one in the liquid-one. Unfortunately, as one can see from Fig. 3.1, there is no such sharp value. So, we firstly chose as  $C$  the average value of the order parameter between an all solid system and an all liquid one, namely:  $(\Phi_s + \Phi_l)/2$ . However, we realized that such value was susceptible of appreciable changes if the interface was moving considerably due to fluctuations (larger in smaller cells) or if we changed the coarse-graining length  $\xi$ . Hence, we had the idea of transforming again the order parameter function by applying a second switching function: this function (see Footnote 3) was tuned so that the resulting order parameter had a really sharp change when traversing the diving surface; in this way, liquid atoms had a value of  $\Phi$  very close to 0 and solid ones almost equal to 1. We could then fix the value of the constant to 0.5<sup>6</sup>.

<sup>4</sup>See [https://en.wikipedia.org/wiki/Brent%27s\\_method](https://en.wikipedia.org/wiki/Brent%27s_method)

<sup>5</sup>Again, practical details on how this average has been calculate will be given when discussing results. Here we just note that, since time is discretized by definition in a MD simulation, we only have snapshots of the fluctuation spectrum and the time interval between two of these is a multiple of the timestep used in the MD simulation. Since an observable in consecutive snapshots may show a correlated behaviour, we exploited a way of computing the average in order to estimate correctly also the error on this average.

<sup>6</sup>Another small, but important detail hides in here: when computing the field as in Eq. (3.5), the distance  $|\mathbf{r} - \mathbf{r}_i|$  refers to a certain coordinate system with a fixed origin. It should be evident that changing the origin will influence the final result for  $\rho_\phi$ . So, in all our analysis, we fixed the origin by computing a weighted average position based on the values of the order parameter. Coordinates of the origin are defined according to

$$x_\alpha = \frac{1}{2\pi} \arctan \left[ \frac{\sum_i w_i \Phi_i \sin(2\pi x_{i,\alpha})}{\sum_i w_i \Phi_i \cos(2\pi x_{i,\alpha})} \right],$$

### 3.1.3 Fitting capillary fluctuations spectrum

To obtain the values of the stiffness tensor  $\sigma$ , the only thing left is fitting the averaged fluctuation spectrum with respect to  $k$ -vector, following the prescription of Eq. (2.4):  $T_m$  is known and the cross sectional area  $S$  is simply the product  $L_x \times L_y$ . The only substantial difference here is a multiplicative term added to the fitting model, which changes into

$$\langle |A(\mathbf{k})|^2 \rangle = \mathcal{P} \frac{\exp(-k^2/2\xi^2)}{k_x^2 \sigma_{11} + k_y^2 \sigma_{22} + 2k_x k_y \sigma_{12}}, \quad (3.8)$$

where  $\mathcal{P} = k_B T_m / S$  is the constant prefactor. To explain why we added the exponential term, we recall that our representation of the surface is the result of a convolution of a Gaussian function with the order parameter density field. It is known that the Fourier transform of a convolution is the pointwise product of Fourier transforms and the Fourier transform of a Gaussian is again a Gaussian with a different width: this is the reason behind our modification of the fitting model.

## 3.2 Results

### 3.2.1 The models

As already explained, the CFM framework adopted allowed us to run only two independent simulations with different interface orientation. Specifically, (100) and (110) interface of an FCC crystal were chosen.

With the aim of verifying our revisited approach, we firstly studied capillary fluctuations in simple Lennard–Jones systems, leaving to future work the study of real alloy systems of concrete interest in additive manufacturing processes.

All the simulations were performed with the molecular dynamics code LAMMPS, together with PLUMED for post-simulation analysis. The potential used was a truncated Lennard–Jones potential [6]:

$$V(r) = \begin{cases} 4\epsilon \left[ \left(\frac{\sigma}{r}\right)^{12} - \left(\frac{\sigma}{r}\right)^6 \right] + C_1 & r \leq 2.3\sigma \\ C_2 \left(\frac{\sigma}{r}\right)^{12} + C_3 \left(\frac{\sigma}{r}\right)^6 + C_4 \left(\frac{\sigma}{r}\right)^2 + C_5 & 2.3\sigma < r < 2.5\sigma \\ 0 & r \geq 2.5\sigma \end{cases} \quad (3.9)$$

where  $C_1 = 0.016132\epsilon$ ,  $C_2 = 3136.6\epsilon$ ,  $C_3 = -68.069\epsilon$ ,  $C_4 = -0.083312\epsilon$  and  $C_5 = 0.74689\epsilon$ . The timestep was set equal to 0.004 time units in the Lennard–Jones scheme. The direction parallel to the interface normal was aligned with the  $z$  axis and throughout all the simulations the  $NP_zT$  ensemble was employed, with the Nose–Hoover thermostat and barostat to control pressure and temperature of the system.

---

where  $w_i$  are weights,  $\Phi_i$  are the values of the order parameter and  $x_{i,\alpha}$  the scaled Cartesian components of the position of the atoms. All the analysis were run within the framework of the software PLUMED, with which is rather easy to compute such a quantity.

The simulations for both the interfaces studied were run at the equilibrium melting temperature of 0.618 (in LJ units) and the initial crystalline systems were prepared considering the equilibrium lattice parameter at that temperature.

Models of both solid–liquid interfaces studied were generated as follows: once the interface of interest had been fixed, a perfect crystalline FCC unit cell was prepared with a lattice parameter consistent with the chosen temperature ( $T_m$ ). The  $z$  axis of the coordinate system was always aligned with the direction indicating the interface normal. Then, the unit cell has been replicated in the  $xy$  plane and along  $z$ , always with a larger number of replicas in the  $z$  direction, to ensure that solid and liquid regions were not too thin and statistical fluctuations too large.

First step of the simulations was actually generating the solid–liquid interface. To this end, a central slab of atoms has been held fixed: the size of this region depended on the length of the supercell in the  $z$  direction (between  $L_z/3$  and  $2L_z/3$ ). A number of simulation steps ( $\approx 25 \times 10^3$ ) were run in  $NPT$  ensemble with the temperature fixed well above  $T_m$ , leading to complete melting of the two side regions of the supercell. Afterwards, the same number of steps were run with the target temperature of the thermostat being again fixed at  $T_m$  and then a number of equilibration steps was carried out, letting all the atoms follow the unconstrained dynamics. With the protocol described, after approximately  $1 \times 10^5$  MD steps, we obtained the equilibrated systems at the melting temperature with coexistence of solid and liquid regions. It is worth noting that no adjustment of the density was necessary when the liquid parts were generated, because the pressure was kept constant by the barostat and the volume was always free to fluctuate.

### 3.2.2 (100) interface

Following the recipe described above, to study (100) interface a supercell of  $20 \times 20 \times 50$  unit cells (in  $x$ ,  $y$  and  $z$  direction respectively) was generated. The total number of atoms is 80 000. Since for an FCC crystal directions in direct space  $[hkl]$  is perpendicular to the surface with the same Miller indexes<sup>7</sup>, the crystallographic axes were aligned along the standard Cartesian coordinate system.

#### Grid spacing and bandwidth

As the (100) model was the first to be studied, we ran preliminary tests changing the two tunable parameters when computing the order parameter field of Eq. (3.5): the coarse–graining length  $\xi$  and the spacing of the grid on which all the distances appearing in Eq. (3.5) were computed<sup>8</sup>. For the grid spacing, we analysed the same trajectory of  $1 \times 10^6$  steps (not counting the steps carried out for preparing the model, as described above) with the following different grid spacings: 0.25, 0.5 and 1.0 (in LJ distance units). We noticed that only 1.0 gave an appreciable

<sup>7</sup>This statement is in general true for Bravais lattices with equal length basis vectors.

<sup>8</sup>In Eq. (3.5) the symbol  $\mathbf{r}$  denotes an arbitrary position with respect to a chosen coordinate system. It is clear that, when computing the distance term in that expression, only a finite set of points in space can be “sampled”: these points are those of a regular 3D grid, built considering the simulation box sizes and the spacing between two consecutive points in each direction.

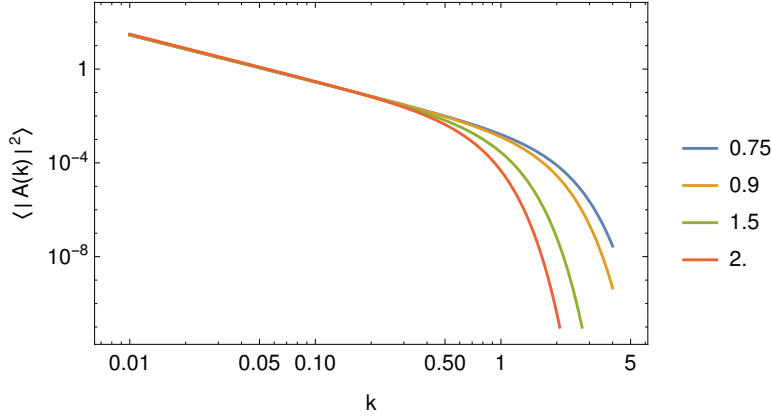


Figure 3.2: Plots of the fitted Fourier spectrum with different values of  $\xi$  used to build the coarse-grained field. Here  $k$  stands for  $k_x$ .

difference in the Fourier spectrum. This parameter controls the total number of grid points (and in turn the number of  $k$  points, but not the smallest wave vector possible, which depends only on the simulation cell size), so a smaller value would mean having just more points for which to compute the distances with all the atoms; a value chosen within a reasonable range<sup>9</sup> does not affect much the result (i.e. the Fourier spectrum). For this reason, all the analysis were done with a grid spacing of 0.5, a value that even for large simulation cells did not result in too expensive calculations.

The coarse-graining length (or bandwidth)  $\xi$  deserves more attention, because this parameter also enters the model used afterwards to fit the Fourier spectrum and obtain the stiffness tensor. We recall that the original model used for the fits is something like  $A(k) \propto 1/k^2$ , while our model has a multiplicative Gaussian term in addition:  $A(k) \propto \exp(-k^2/2\sigma_k^2)/k^2$ . As we built our order parameter density field by means of a convolution, Fourier transforming a Gaussian gives another Gaussian in  $k$  space with the only difference in the bandwidth. Specifically, it holds the relation  $\sigma_k = 1/\sigma$ . Thus, we expect that a change in the  $\xi$  used to build the coarse-grain field will influence the region of  $k$  space over which the Gaussian smoothening shows its effect; in particular, the larger  $\xi$ , the narrower this region will be. As Fig. 3.2 shows, this is exactly what we obtained.

### Computing the average Fourier spectrum

As explained in the Method section, the quantity subject to the fit as a function of  $\mathbf{k}$  vectors is the average Fourier spectrum,  $\langle |A(k_x, k_y)|^2 \rangle$ . The easiest approach to compute this quantity, assuming valid the ergodicity postulate, would be to calculate for each  $\mathbf{k}$  vector the time average of the corresponding Fourier amplitude (the square modulus of it). With this average it is also straightforward to compute the standard error of the mean.

The problem arises when dealing with time correlated data. Since we are studying fluctua-

<sup>9</sup>“Big” is far from specific, obviously: we can say that big would mean choosing a value much larger than the average distance between atoms; this choice would lead to a very coarse grid poorly sampling the simulation box.

tions in Fourier spectrum,  $\langle |A(\mathbf{k}, t)|^2 \rangle$  is a clear example of data correlated in time. There are many ways to compute the correct error estimate of data of this kind. The main one consists of computing the so-called time auto-correlation function of the data set; the problem is that computing time correlation functions is usually expensive and requires a very frequent sampling (on the time scale) of the data. Another way of estimating statistical errors is studying the behaviour of so-called block averages [16].

What we did is a sort of combination of these two methods: since computing the time correlation function for every  $\mathbf{k}$  point would have been too expensive, we considered only those  $\mathbf{k}$  vectors with a zero component, namely  $(2\pi j_x/L_x, 0)$  and  $(0, 2\pi j_y/L_y)$ . We then calculated the fundamental quantity of auto-correlation time,  $\tau$ , which gives an estimate of how long one would have to “wait” between two consecutive samples of the measured observable to collect uncorrelated measures of it. Then, we used this information to compute the proper average and corrected error following the “block average” algorithm.

The idea of the block average is the following [17]: let  $A_1, A_2, \dots, A_L$  be  $L$  consecutive samples of the quantity we want to calculate the average and its error. We now group our data in the following way

$$A'_i = (A_{2i-1} + A_{2i})/2 \quad (3.10)$$

with  $L' = 0.5L$ . Clearly, the average of this “new” set of data is unchanged. The variance of this new set is given by

$$\sigma^2(A') = \langle A'^2 \rangle - \langle A' \rangle^2 = \frac{1}{L'} \sum_{i=1}^{L'} A_i'^2 - \bar{A}_i'^2. \quad (3.11)$$

If we perform again this blocking operation (taking instead of couple of data, group of three) and if we have a simulation long enough, the averages  $A'_i$  will become completely uncorrelated. This means that the following relation would hold

$$\frac{\sigma^2(A')}{L' - 1} \approx \text{constant}. \quad (3.12)$$

In a similar way, we can also determine the statistical error of  $\sigma^2(A')$ , which would give an estimate of the variance in our ensemble average

$$\sigma^2(A) \approx \frac{\sigma^2(A')}{L' - 1} \pm \sqrt{\frac{2\sigma^4(A')}{(L' - 1)^3}}. \quad (3.13)$$

In our case, we have also an estimate of what is the auto-correlation time  $\tau$ , so we can avoid the full block average calculation and compute the error given by Eq. (3.13) with a block size  $L'$  corresponding to a time interval of  $\sim \tau$ . In this way the final ensemble average will have an error estimate appropriately adjusted taking into account time correlation.

Table 3.1: Stiffness values calculated by our method at 0.6185 reduced temperature for (100) and (110) interfaces. Units on stiffness are  $(\epsilon/\sigma^2)$ . The values obtained by Becker at the same temperature are also reported for comparison (95% confidence level on the last digit).

Interface ( $hkl$ )	Present work			Ref. [18]
	$\sigma_{11}$	$\sigma_{22}$	$\sigma_{12}$	$\sigma$
(100)	$0.2897 \pm 8.0 \times 10^{-4}$	$0.2871 \pm 7.0 \times 10^{-4}$	$4.6 \times 10^{-18}$	0.2866
(110)	x	y	z	other

#### Stiffness tensor for (100)

Having explained all the technical details, we present in this section the results for the stiffness tensor obtained in our simulations. According to the analysis explained in the previous section, the average of the Fourier spectrum and its error estimates were computed considering blocks of 72 frames.

Since (100) is a highly symmetric surface for the FCC system, it can be shown that the following relations hold for the stiffness tensor,  $\sigma$ :  $\sigma_{11} = \sigma_{22}$  and  $\sigma_{12}$  is zero. Table 3.1 summarizes the results obtained and compares them with the values of Becker et al. [18]<sup>10</sup>.

#### 3.2.3 (110) interface

The model used to study (110) interface was prepared in the same way as the one for the (100); the only differences are the number of unit cells for each direction of the supercell ( $20 \times 20 \times 30$ ) and the directions along which the Cartesian axes were aligned:  $x$  axis is along  $[\bar{1}10]$ ,  $y$  along  $[001]$  and  $z$  along  $[110]$ , that is the normal to the interface (110). Incidentally, this is the same configuration adopted by Becker et al. [18].

<sup>10</sup>In this work, the fitting model is a symmetry-consistent model, that is for the (100) only one value of the stiffness tensor was considered. The model is identical to the one used for one-dimensional interfaces.

## 4 | Modeling atomistic interactions

### 4.1 The embedded atom method

In recent years, our knowledge of the atomic structure of solids and their physical properties has advanced considerably both from theoretical and experimental points of view. More versatile and powerful methods in computational science allowed the possibility of investigate more deeply properties and phenomena of condensed matter; this has been possible also thanks to the growing computers' power. From the experimental side, it is now possible to resolve with very high accuracy the atomic scale structure of complex system like interfaces, surfaces, and grain boundaries. Lastly, but not less important, the broad class of first principles calculations, such as the well-known density functional theory, are capable of explaining complex and basic properties that years ago were only took into account as approximations.

Despite all this huge progress, many systems of interest for a variety of scientific fields are still too complex and demand reliable but approximate methods. All the relevant properties of matter in any of its forms arise from the interactions among its constituents, be them atoms, molecules or macromolecules such as proteins or polymers. A unique way of explaining all these possible interactions is both impossible and useless, because one would have to deal with an enormous quantity of informations.

The very first approach to model interactions involves the class of pair potentials (the Lennard-Jones potential is the easiest example). Although this potentials can be useful to model very simple system or to give a rough approximation of some kind of fundamental interaction, the pair potential scheme has been shown to fail in describing the physics of metallic bonding. This kind of interaction is undoubtedly a fundamental one because of the vast numbers of elements and compounds that show metallic behaviour.

Most of the questions regarding structure and thermodynamics of condensed matter system can be answered from the knowledge of the total energy. The total energy of a solid can be determined, at least in principle, by solving the many-electron Schrödinger equation, but this problem is overwhelming in practice and some approximations are needed to reduce the complexity without losing the important physics. The scheme of pair interactions is clearly the most extreme approximation and it easy to show why it falls short. If we take the cohesive energy to be a sum only over pair bonds,

$$E_{\text{coh}} = \frac{1}{2} \sum_{i \neq j} V(R_{ij}), \quad (4.1)$$

it is evident that bonds between atoms are independent of each other. This assumption is very simple and can be also very useful, but it has the major difficulty that it is not possible to show theoretically that the total energy can be written as a sum over pairs. The error stems from the fact that, in general, bonds between atoms are not independent of each other. To be more concrete, it is sufficient to look at a table of cohesive energy measured experimentally for crystal structures that differ only by the coordination  $Z$  of a typical atom: the pair model of Eq. (4.1) predicts that the cohesive energy scales linearly with  $Z$  ( $E_{\text{coh}} \propto -Z$ ), but in reality the energy scales more weakly with a power law like  $-Z^{1/2}$ : this means that the strength of an additional bond is not constant, but rather decreases with increasing  $Z$ .

The very simple argument stated above seems to suggest that the key to understand many of the interesting problems in the structure of solids (and in particular of metals) lies in coordination-dependent interactions. It was with this idea in mind that Daw and Baskes in 1983 [19, 20] proposed the *embedded atom model* (EAM). In this scheme, the total energy of a metal is a sum of energies obtained by inserting an atom into the local electron density produced by the remaining atoms of the system. Since we are dealing with charged particles, there is an additional pair term that takes into account electrostatic interaction. The expression for the total energy  $E_i$  of the  $i$ -th atom within EAM is

$$E_i = F_\alpha \left( \sum_{j \neq i} \rho_\beta(r_{ij}) \right) + \frac{1}{2} \sum_{j \neq i} \phi_{\alpha\beta}(r_{ij}). \quad (4.2)$$

Here  $F$  is the embedding energy, defined as the interaction of the atom  $i$  of type  $\alpha$  with the background electron gas;  $\rho_\beta$  is the spherically averaged atom electron density and  $\phi$  is an electrostatic, two-atom interaction. The background density for each atom is determined by evaluating at its nucleus the superposition of atomic density tails from the other atoms.

In 1984, Finnis and Sinclair [21] proposed a more general way of computing the total energy term  $E_i$ ,

$$E_i = F_\alpha \left( \sum_{j \neq i} \rho_{\alpha\beta}(r_{ij}) \right) + \frac{1}{2} \sum_{j \neq i} \phi_{\alpha\beta}(r_{ij}). \quad (4.3)$$

This has the same form as Eq. (4.2), except that  $\rho$  is now a functional specific to the atomic types of both atoms  $i$  and  $j$ . In this way distinct elements can contribute differently to the total electron density at an atomic site depending on the chemical species of the element at that particular atomic site.

One interesting aspect of EAM is its physical description of the metallic bonding: each atom is embedded in an host electron gas created by its neighboring atoms. The atom-host interaction is inherently more complex than the simple two-body picture of the pair-bond model. In this way the embedding functions  $G$  can incorporate some important effects which arise only from considering many-body interactions.

Currently, EAM is the first choice for doing semi-empirical calculations in close-packed metals and related compounds such as alloys. The EAM combines the computational simplicity needed



for large systems with a physical description of the underlying interactions that includes many-body effects, which are completely ignored in a pair-bond model.

To conclude this very quick theoretical overview of EAM, in the review work of Das, Foiles and Baskes [22] a series of examples for which the EAM has been successfully applied are cited and thoroughly discussed.

## 4.2 Applications to alloys

EAM potentials have been applied to study various properties of alloyed metals, such as the compositional variations that can occur near defects. The main advantage of EAM over other approaches is that the interaction of one atom with the electron gas does not depend on the origin of the latter, but it is rather assumed to depend only on the local electron density. A change in the chemical identity of the neighbors enters the problem through a change in the electron densities (i.e. the functions  $\rho_{\alpha\beta}$ , in the generalized expression); this means that the embedding function used for pure metals should still be valid for the case of alloys. However, even though in the original work of Daw and Baskes [20] were given mixing rules to obtain  $\rho_{\alpha\beta}$  and  $\phi_{\alpha\beta}$  for any alloy once known the corresponding functions for the elemental systems, it was soon made clear that this approximation was not enough to produce reliable and transferable potentials with the desired accuracy and the EAM was then revisited to include directly the fit to properties of the complex system of interest.

One should also be aware of possible errors when applying EAM potentials to complex systems like alloys. Large charge transfers in an alloy will be poorly described in the EAM, as well any effect arising from subtleties of the Fermi surface, that are completely ignored in the EAM.

This section will present some useful and recent applications of the EAM to study different properties of metal alloys, with a particular focus on nickel and gold alloys.

### 4.2.1 Nickel ternary alloys

As described previously, Ni-based superalloys are subject of many studies for their high performance applications as structural materials with excellent strength and creep resistance. These alloys are generally made of Ni, Ti and Al and the precipitation of the  $\gamma'$  ordered phase within the Ni FCC matrix is mainly responsible for the high strength. Also, plasticity response is thought to be due to formations of defects such as vacancies and impurities that affect dislocations motion. For all these reasons, it is interesting to have a method to simulate and understand the underlying processes on the atomic-scale.

The study of nickel ternary alloys typically requires reliable potentials to model interactions between Ni-Al, Ni-Ti and Al-Ti. The Ni-Al system has been widely studied and several EAM potentials have been developed [23], based both on the  $\text{Ni}_3\text{Al}$  system [24, 25] and on NiAl system [26, 27]. For this ternary system some complications arise from the Ti-Al case, for which the EAM fails in reproducing correctly the elastic constants due to the presence of non central forces<sup>1</sup>. Farkas [28] has developed and compared interatomic potentials for the Ti-Al

<sup>1</sup>Ref. 6 ibidem

system that included the non-central terms as well as a best possible potential without the angular term. In that work, Farkas showed that the main contribution of including central interactions was in the elastic constants, while total energy and stacking faults energies of various phases of Ti–Al system varied much less.

When dealing with alloys of three (or even four) components, the EAM presents a practical advantage: the pairwise term involves only two atoms at a time and therefore can be calculated from the binary interactions involved in the ternary system in question. The embedding functions are defined separately for each of the components of the system and does not require any additional fitting beyond that done for pure components. Also the local electronic density depends only on the strength of each individual contributions of each of the three components. It follows that if EAM potentials are available for the three binary systems involved in a particular ternary, it is in theory possible to describe also the ternary system. The only requirement is that the interatomic interaction used for each of the pure components in the description of the two binaries involving that constituent be the same.

In the work of Mishin in 2004 [29], a new EAM potential has been developed for the Ni<sub>3</sub>Al system, by fitting to both experimental and first-principles data. A series of recent works, aimed also to understanding the role of defects formation in plasticity response of Ni ternary alloys [30], have considered this new potential to be among the most reliable ones for modeling  $\gamma + \gamma'$  phases on Ni superalloys, with good accuracy in predicting  $\gamma/\gamma'$  interface energy.

Lastly, a ternary potential for the system Ni–Al–W has been constructed by Fan et al. [31] for the Ni-based single crystal superalloys to model the doping of Ni–Al system with tungsten, also comparing results with other calculations when the doping element were Re or Co<sup>2</sup>.

Results obtained with this potential were in good agreement with experiment; for example, the potential predicts that the solute atoms of W does not form cluster within the  $\gamma$  phase, which is consistent with experiments. Also, increasing the addition of W, the lattice misfit between the two phases decreases and the elastic constants of the  $\gamma'$  phase increase.

To conclude this part on EAM applied to Ni and alloys, two tables are reported: the first one summarizes the results of Mishin [29] on lattice properties of Ni and Al calculated with the EAM potential there developed; in the table are also present experimental data [32–34]. The second one shows the predicted equilibrium energies of different structures of Ni and Al with the EAM potential of Mishin, in comparison with first-principles calculations.

### 4.2.2 Gold and its alloys

Literature on EAM potential on gold and related alloys is less numerous than nickel (or titanium), especially when going beyond the simple metal system. Nevertheless, as we explained previously, the EAM framework allows to combine different single-element potentials, that should reproduce as best as possible the interested properties, and build from these an effective potential for the complex system under study, for example a ternary alloy.

With this in mind, the table below is taken from the recent work of Grochola et al. [35], in which a new EAM potential for gold is developed, using an improved methodology to fit to

---

<sup>2</sup>W, Re, Co, Mo and Va are common additives for Ni superalloys since they behave as solid-solution strengtheners both for  $\gamma$  and  $\gamma'$  phases.

Table 4.1: Lattice properties of Ni and Al calculated with the potential developed by Mishin [29] in comparison with experimental data.

Property	Ni		Al	
	Experiment	EAM	Experiment	EAM
$a_0$ (nm)	0.352	0.352	0.405	0.405
$E_0$ (eV)	-4.45	-4.45	-3.36	-3.36
<i>Elastic constants</i> (GPa):				
$B$	181.0	181.0	79.0	79.0
$c_{11}$	246.5	241.3	114.0	116.8
$c_{12}$	147.3	150.8	61.9	60.1
$c_{44}$	124.7	127.3	31.6	31.7

high-temperature solid lattice constants and liquid densities. This new potential shows an appreciable overall improvement in the agreement with several experimental data, in comparison with previous potentials of Foiles et al. [36], Johnson [37] and the glue model potential of Ercolessi et al [38]. Grochola and coworkers emphasize how attempting a fit to *all* the properties for which an experimental data is available is by far unsuccessful. However, the results obtained for gold suggest that for other metal species further overall improvements in potentials may still be possible within the EAM framework with an improved fitting methodology.

Table 4.2: Equilibrium energies (in eV) for different stable structures of Ni and Al predicted by the EAM potential developed by Mishin [29], compared to first-principles calculations.

Structure	Ni		Al	
	Ab initio	EAM	Ab initio	EAM
HCP	0.03	0.03	0.04	0.03
BCC	0.11	0.07	0.09	0.09
$L1_2$	0.66	0.54	0.27	0.33
SC	1.00	0.72	0.36	0.30
Diamond	1.94	1.42	0.75	0.88

## Chapter 4. Modeling atomistic interactions

---

Table 4.3: Comparison table between predicted values of EAM potentials for gold discussed (and referenced) in this section. The table is partially reproduced from Grochola et al [35]. Units: elastic constants in GPa, energies in eV and lattice parameters in Å.

Property	Potential developped by				Exp.
	Grochola	Ercolassi	Johnson	Foiles	
Cohesive energy	-3.924	-3.78	-3.930	-3.927	-3.93
Lattice constant	4.0701	4.0704	4.0806	4.0805	4.07
Bulk modulus	1.8026	1.8037	1.6987	1.6673	1.803
$c_{11} - c_{12}$	0.3207	0.5998	0.2687	0.2454	0.319
$c_{44}$	0.4594	0.5998	0.4069	0.4524	0.454
Melting point (K)	1159	1338	1053	1121	1337

## 5 | Outlook

### 5.1 CFM out of equilibrium

Lorem ipsum dolor sit amet, consectetur adipiscing elit. Ut purus elit, vestibulum ut, placerat ac, adipiscing vitae, felis. Curabitur dictum gravida mauris. Nam arcu libero, nonummy eget, consectetur id, vulputate a, magna. Donec vehicula augue eu neque. Pellentesque habitant morbi tristique senectus et netus et malesuada fames ac turpis egestas. Mauris ut leo. Cras viverra metus rhoncus sem. Nulla et lectus vestibulum urna fringilla ultrices. Phasellus eu tellus sit amet tortor gravida placerat. Integer sapien est, iaculis in, pretium quis, viverra ac, nunc. Praesent eget sem vel leo ultrices bibendum. Aenean faucibus. Morbi dolor nulla, malesuada eu, pulvinar at, mollis ac, nulla. Curabitur auctor semper nulla. Donec varius orci eget risus. Duis nibh mi, congue eu, accumsan eleifend, sagittis quis, diam. Duis eget orci sit amet orci dignissim rutrum.



# Bibliography

- [1] C. S. Wright et al. In: *Mater. Sci. Forum* 514–516 (2006), pp. 516–523.
- [2] T. H. C. Childs, C. Hauser, and M. Badrossamay. In: *Proc. Inst. Mec. Eng.* 219B (2005), pp. 339–357.
- [3] D. Becker, W. Meiners, and K. Wissenbach. “Additive manufacturing of copper alloys by selective laser melting”. In: *Lasers in Manufacturing*. WLT, June 2009, pp. 195–199.
- [4] A. Simchi, F. Petzoldt, and H. Pohl. In: *J. Mater. Process. Technol.* 141 (2003), pp. 319–328.
- [5] S. Angioletti–Uberti et al. “Solid–liquid interface free energy through metadynamics simulations”. In: *Phys. Rev. B* 81 (2010), p. 125416.
- [6] Bingqing Cheng, Gareth A. Tribello, and Michele Ceriotti. “Solid-liquid interfacial free energy out of equilibrium”. In: *Phys. Rev. B - Condens. Matter Mater. Phys.* 92.18 (2015), pp. 1–5. DOI: 10.1103/PhysRevB.92.180102.
- [7] J. J. Hoyt, Mark Asta, and Alain Karma. “Method for Computing the Anisotropy of the Solid-Liquid Interfacial Free Energy”. In: *Phys. Rev. Lett.* 86 (2001), pp. 5530–5533.
- [8] S.W. Sides, G.S. Grest, and M.D. Lacasse. In: *Phys. Rev. E* 60 (1999), p. 6708.
- [9] T. Hapke, G. Patzold, and D.W. Heermann. In: *J. Chem. Phys.* 109 (1998), p. 10075.
- [10] J J Hoyt, M Asta, and A Karma. “Atomistic and continuum modeling of dendritic solidification”. In: *Mat. Sci. Eng. R* 41 (2003), pp. 121–163.
- [11] A Karma. “Fluctuations in solidification”. In: *Phys. Rev. E* 48.5 (1993), pp. 3441–3458.
- [12] W.R. Fehlner and S.H. Vosko. In: *Can. J. Phys.* 54 (1976), p. 2159.
- [13] C A Becker et al. “Atomistic Underpinnings for Orientation Selection in Alloy Dendritic Growth”. In: 125701.March (2007), pp. 98–101.
- [14] P. J. Steinhardt, D. R. Nelson, and M. Ronchetti. In: *Phys. Rev. B* 28 (1983), p. 784.
- [15] Adam P Willard and David Chandler. “Instantaneous liquid interfaces”. In: *J. Phys. Chem. B* 114.5 (2010), pp. 1954–1958.
- [16] D. Frenkel and B. Smit. *Understanding molecular simulation*. Academic Press, 2002.
- [17] H. Flyvbjerg and H.G. Petersen. “Error estimates on averages of correlated data”. In: *J. Chem. Phys.* 91 (1989), pp. 461–466.

## Bibliography

---

- [18] C. A. Becker et al. “Atomistic simulations of crystal–melt interfaces in model binary alloys: Interfacial free energies, adsorption coefficients and excess entropy”. In: *Phys. Rev. B* 79 (2009), p. 054109.
- [19] M.S. Daw and M.I. Baskes. In: *Phys. Rev. Lett.* 50 (1983), p. 1285.
- [20] M.S. Daw and M.I. Baskes. In: *Phys. Rev. B* 29 (1984), p. 6443.
- [21] M. W. Finnis and J. E. Sinclair. “A simple empirical N-body potential for transition metals”. In: *Philosophical Magazine A* 50.1 (1984), pp. 45–55.
- [22] Murray S. Daw, Stephen M. Foiles, and Michael I. Baskes. “The embedded-atom method: a review of theory and applications”. In: *Mater. Sci. Reports* 9.7-8 (1993), pp. 251–310.
- [23] R Pasianot et al. In: *Modelling Simulation Mater. Sci. Eng.* 2 (1994), p. 383.
- [24] S M S. Foiles and Murray S. Daw. In: *J. Mater. Res.* 2 (1987), p. 5.
- [25] A. Voter and S. Chen. “Accurate interatomic potentials for Ni, Al and Ni<sub>3</sub>Al”. In: *Materials Research Society Symp.* Vol. 82. 1987, pp. 175–180.
- [26] D. Farkas et al. In: *Modelling Simulation Mater. Sci. Eng.* 3 (1995), p. 201.
- [27] A. Rao, C. Woodward, and T. Parthasarathy. “Empirical interatomic potentials for L10 TiAl and B2 NiAl”. In: *Materials Research Society.* Vol. 213. 1991, pp. 125–130.
- [28] D. Farkas. “Interatomic potentials for Ti-Al with and without angular forces”. In: *Model. Simul. Mater. Sci. Eng.* 2 (1994), pp. 975–984.
- [29] Y. Mishin. “Atomistic modeling of the  $\gamma$  and  $\gamma'$ -phases of the Ni-Al system”. In: *Acta Mater.* 52.6 (2004), pp. 1451–1467.
- [30] F Bianchini, J R Kermode, and A De Vita. “Modelling defects in Ni–Al with EAM and DFT calculations”. In: *Model. Simul. Mater. Sci. Eng.* 045012 (2016), p. 45012.
- [31] Qin Na Fan et al. “A ternary Ni-Al-W EAM potential for Ni-based single crystal super-alloys”. In: *Phys. B Condens. Matter* 456 (2015), pp. 283–292.
- [32] R.C. Weast, ed. *Handbook of chemistry and physics*. CRC Press, 1984.
- [33] G. Simmons and H. Wang. *Single crystal elastic constants and calculated aggregate properties*. MIT Press, 1977.
- [34] *Metals: phonon states, electron states, and Fermi surfaces*. Landolt-Bornstein, Springer, 1981.
- [35] G. Grochola, S. P. Russo, and I. K. Snook. “On fitting a gold embedded atom method potential using the force matching method.” In: *J. Chem. Phys.* 123.20 (2005), p. 204719.
- [36] S. M. Foiles, M. I. Baskes, and M. S. Daw. “Embedded-atom-method functions for the fcc metals Cu, Ag, Au, Ni, Pd, Pt, and their alloys”. In: *Phys. Rev. B* 33 (12 June 1986), pp. 7983–7991.
- [37] R. A. Johnson. “Analytic nearest-neighbor model for fcc metals”. In: *Phys. Rev. B* 37 (1988), pp. 3924–3931.



- [38] F. Ercolessi, M. Parrinello, and E. Tosatti. “Simulation of gold in the glue model”. In: *Philosophical Magazine A* 58.1 (1988), pp. 213–226.